Eikonal method for charge-exchange reactions at intermediate energies

J. J. Li,[1,5,*] C. A. Bertulani,[2] Y. Liu,[1] J. L. Lou,[1] D. Y. Pang,[3,4] X. H. Sun,[1] B. Yang,[1] X. F. Yang,[1] and Y. L. Ye[1,*]

[1]*School of Physics and State Key Laboratory of Nuclear Physics and Technology, Peking University, Beijing 100871, China*

[2]*Department of Physics and Astronomy, Texas A & M University-Commerce, Commerce, Texas 75429, USA*

[3]*School of Physics, Beihang University, Beijing 100191, China*

[4]*Beijing Key Laboratory of Advanced Nuclear Materials and Physics, Beihang University, Beijing 100191, China*

[5]*Research Center of Laser Fusion, China Academy of Engineering Physics, Mianyang 621900, China*

(Received 9 March 2020; accepted 10 November 2020; published 1 December 2020)

A novel description of charge-exchange reactions at intermediate energies is developed, based on both phenomenological or microscopic eikonal phase-shift functions. The results obtained within this eikonal approach are in good agreement with the distorted-wave Born approximation calculations within the energy region where both approximations should be valid. They also compare well with the experimental data, even at relatively low energy domain. At higher energies, relativistic kinematics have also been added and shown to be relevant. Owing to the microscopic feature of the formulation, our theory also has the advantage that it can be applied to high energies where the phenomenological optical potentials are rarely available.

DOI: 10.1103/PhysRevC.102.064601

I. INTRODUCTION

Charge-exchange (CE) reactions, with hadronic probes such as (p, n), (^{3}He, t), (^{12}C, ^{12}N) reactions, have been widely used as one of the most sensitive tools for nuclear structure studies. The related studies include the determination of (a) Gamow-Teller (GT) transition strength in excitation-energy regions inaccessible by β decay [1–4], (b) spin-dipole transition strengths [3], (c) properties of isovector giant resonances [2,5], (d) symmetry energy [2,6], (e) the isospin symmetry breaking in asymmetric nuclear matter [6–8], and (f) the Landau-Migdal parameter [8]. In particular, GT strengths are crucial for understanding various problems in stellar evolution, such as neutrino induced nucleosynthesis and neutrinoless double-β decay [1,3,8]. We now know that heavy-ion probes allow a better extraction of the GT strength, compared with (p, n) reactions, because of higher energy resolution and to a collective participation of nucleons at the surface of the target nucleus [1–4].

In recent years, more attention was paid to experimental studies of CE reactions at intermediate and high energies ($\geqslant$100 MeV/nucleon), owing to renewed interests for the above mentioned physics problems [2,3,8]. Prior studies indicate that the reaction mechanism at these energies is dominated by one-step processes. Hence, precise extraction of the weak transition strengths or other nuclear structure information can be achieved, as long as appropriate theoretical tools are applied to describe the reaction process [9]. However, so far few theoretical formulations exist at the intermediate and high energy domain [4,10,11], although at lower energies ($<$100 MeV/nucleon) CE reactions can be successfully reproduced by the conventional distorted-wave Born approximation (DWBA) calculations [12–16]. It is difficult to apply the latter at higher energies, because the required phenomenological potential, namely the optical potential (OP), is rarely available there [4,17]. In addition, the Schrödinger equation determining the distorted waves is not valid at relativistic energies. To overcome these difficulties, we use the eikonal formalism which can be formulated microscopically by using well-known nucleon densities and nucleon-nucleon (NN) interactions [18]. The present work includes the complete formulation and the code implementation. The differential cross sections (DCS) calculated within this eikonal approach (EA) are in excellent agreement with those from conventional DWBA calculations, for CE reactions up to 140 MeV/nucleon. It also provides a good description of the experimental data. This eikonal method, together with the relativistic kinematics, can also be applied to CE reactions up to a few GeV energy range.

This article is mainly composed of two parts: theoretical formulation and benchmark calculations. The theoretical section is devoted to the derivation of the detailed EA formulation for CE reactions. In the calculation section, we compare results from EA and with those from DWBA, discuss the effects of tensor and exchange terms within EA, and also introduce the relativistic kinematics. Comparisons with experimental data on DCS are also supplemented. Finally, a brief summary is given at the end of the article.

II. THEORETICAL FORMULATION

The DCS for the CE reaction A(a, b)B is usually expressed in the form [17,19],

$$\frac{d\sigma}{d\Omega}(\theta) = \frac{1}{(2J_{\rm A}+1)(2J_{\rm a}+1)} \sum_{\substack{M_{\rm a}M_{\rm b}\\ M_{\rm A}M_{\rm B}}} |f(\theta)|^2, \qquad (1)$$

*1459427301@qq.com; yeyl@pku.edu.cn

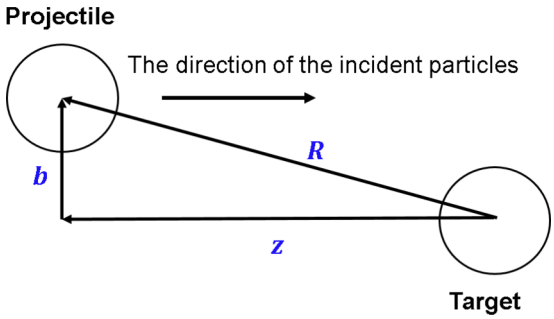

FIG. 1. A schematic view of the cylindrical coordinate system used in the text.

where J_i and M_i stand for the spin and magnetic quantum numbers of the particle i (i = a, b, A, and B), respectively. At intermediate energies, the scattering amplitude $f(\theta)$ can be calculated in the DWBA approach in terms of the interaction matrix element [17,19],

$$f(\theta) = -\frac{\mu}{2\pi\hbar^2}\langle \chi^{(-)}_{k'}(\boldsymbol{R})\Phi_b\Phi_B|V|\Phi_a\Phi_A\chi^{(+)}_{k}(\boldsymbol{R})\rangle, \quad (2)$$

where μ is the reduced mass of the reaction system, $\chi^{(\pm)}(\boldsymbol{R})$ is the incoming (+) or outgoing (−) distorted wave function, $\boldsymbol{k}(\boldsymbol{k'})$ the initial (final) relative momentum, and $\boldsymbol{R}$ the vector of the relative position between a and A or b and B. In the equation, Φ is the internal wave function and V the effective interaction potential which induces the charge exchange.

According to the eikonal approximation which is valid at intermediate and high incident energies [17,19], $f(\theta)$ in Eq. (2) becomes

$$f(\theta) = -\frac{\mu}{2\pi\hbar^2}\int d\boldsymbol{R}\, e^{-i\boldsymbol{q}\cdot\boldsymbol{b}}\, e^{i\chi(\boldsymbol{b})}F(\boldsymbol{R}). \quad (3)$$

Here, a cylindrical coordinate system is adopted so that $\boldsymbol{R}$ can be replaced by $\boldsymbol{b} + z\boldsymbol{e}_z$, as shown in Fig. 1. The z axis is parallel to the direction of the incident particles, and the vector in the plane perpendicular to the z axis, $\boldsymbol{b}$, is generally called the impact parameter. In the equation, the transferred momentum $\boldsymbol{q}$ is equal to $\boldsymbol{k'} - \boldsymbol{k}$ as illustrated in Fig. 2, with $q \approx 2k\sin(\theta/2)$.

In Eq. (3), the phase shift function $\chi(\boldsymbol{b})$ is defined as

$$\chi(\boldsymbol{b}) = -\frac{\mu}{\hbar^2 k}\int_{-\infty}^{+\infty} U(\boldsymbol{b}, z)dz, \quad (4)$$

where U is the effective interaction potential between the initial particles a and A or the final particles b and B. Generally,

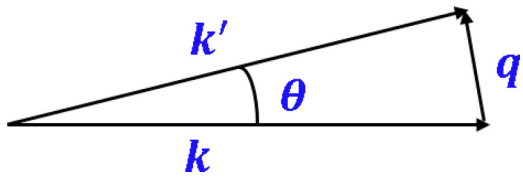

FIG. 2. The definition of the scattering angle θ: the angle between the final momentum $\boldsymbol{k'}$ and the initial momentum $\boldsymbol{k}$. $\boldsymbol{q}$ is the transferred momenta.

the potential U incorporates the nuclear and Coulomb part and $\chi(\boldsymbol{b})$ is the sum of the nuclear and Coulomb phases, χ_N and χ_C, respectively. Quite often, the effective nuclear potential is represented by a phenomenological optical potential U_{OP} in the form [20]:

$$U_{OP}(r) = \frac{V_R}{1 + e^{\frac{r-r_R}{a_R}}} + i\frac{V_I}{1 + e^{\frac{r-r_I}{a_I}}}, \quad (5)$$

where the subscript R or I denotes the real or imaginary potential parameters, respectively, of which the values might be found in the literature.

Instead of a phenomenological U_{OP} [Eq. (5)], a microscopic "$t''_{\rho\rho}$ interaction [19] can be adopted to calculate χ_N, yielding

$$\chi_N(b) = \frac{1}{k_{NN}}\int_0^\infty dq\, q\rho_p(q)\rho_t(q)f_{NN}(q)J_0(qb), \quad (6)$$

where ρ_p and ρ_t are the nucleon densities of the projectile and target, respectively. Here, f_{NN} is the NN scattering amplitude expressed in the following:

$$f_{NN} = \frac{k_{NN}\sigma_{NN}(i + \alpha_{NN})}{4\pi}e^{-\gamma_{NN}q^2}, \quad (7)$$

where k_{NN}, σ_{NN}, α_{NN}, and γ_{NN} are taken from nucleon-nucleon scattering experiments [11]. Using this method, the EA approach can be extended to high incident energies (even beyond 1 GeV) where the phenomenological potential U is not available [11].

In Eq. (3), $F(\boldsymbol{R})$, the form factor carrying the nuclear structure information, is defined by

$$F(\boldsymbol{R}) = \langle J_B T_B J_b T_b \mid V \mid J_A T_A J_a T_a\rangle, \quad (8)$$

where T_i is the isospin of the nucleus i (i = a, b, A, and B), and V is the residual interaction potential (CE interaction potential). The detailed expressions and deductions related to the CE interaction are given in Appendix.

The numerical calculations can be implemented by writing the amplitude $f(\theta)$ in momentum space as

$$\begin{aligned} f(\theta) &= -\frac{\mu}{2\pi\hbar^2}\int d\boldsymbol{b}\, dz\, e^{-i\boldsymbol{q}\cdot\boldsymbol{b}}e^{i\chi(\boldsymbol{b})}\int d\boldsymbol{p}\, e^{-i\boldsymbol{p}\cdot\boldsymbol{R}}F(\boldsymbol{p}) \\ &= -\frac{\mu}{2\pi\hbar^2}\int d\boldsymbol{b}\, dz\, e^{-i\boldsymbol{q}\cdot\boldsymbol{b}}e^{i\chi(\boldsymbol{b})}F(\boldsymbol{R}), \end{aligned} \quad (9)$$

where $F(\boldsymbol{p})$ is the product of all functions of $\boldsymbol{p}$, coefficients in Eq. (A22) except for $e^{-i\boldsymbol{p}\cdot\boldsymbol{R}}$, and coefficients in Eq. (A7).

$e^{-i\boldsymbol{p}\cdot\boldsymbol{R}}$ in Eq. (9) can be expanded into a partial wave series using Eq. (A21). Then $F(\boldsymbol{R})$ in Eq. (9) becomes

$$F(\boldsymbol{R}) = \sum_{\substack{JSL_{tr}\\ M_{tr}}} i^{-L_{tr}}Y^*_{L_{tr}M_{tr}}(\boldsymbol{R})F^{JSL_{tr}}_{M_{tr}}(R). \quad (10)$$

Here the radial form factor $F^{JSL_{\rm tr}}_{M_{\rm tr}}(R)$ has the form,

$$F^{JSL_{\rm tr}}_{M_{\rm tr}}(R) = \sum_{\substack{Ks_0\\ t_0n_0}}\sum_{\substack{l_1l_2\\ l_{12}}} \frac{i^{l_1-l_2+K}}{(2\pi)^3} A^K_{s_0} P^{l_1l_2}_{J_{\rm A}J_{\rm a}M_{\rm a}M_{\rm A}} \hat{J}_{\rm b}\hat{J}_{\rm B}\hat{l}_{12}\hat{K} \times \frac{\hat{l}_1\hat{l}_2\hat{K}}{\hat{L}_{\rm tr}} I^{J_{\rm A}J_{\rm B}J_{\rm a}J_{\rm b},l_2l_1l_{12}}_{JSL_{\rm tr}M_{\rm tr},s_0K} \int p^2 dp\, j_{L_{\rm tr}}(pR) \times \tilde{V}^K_{s_0t_0}(p) D^{l_1s_0J}_{\rm AB}(p) D^{l_2s_0S}_{\rm ab}(p), \quad (11)$$

where $V^K_{s_0t_0}(p)$ [Eqs. (A15) and (A16)], $D^{l_1s_0J}_{\rm AB}(p)$, and $D^{l_2s_0S}_{\rm ab}(p)$ are the NN interaction strength function, transition densities for the target [Eq. (A23)], and that for the projectile, respectively. Detailed information for $A^K_{s_0}$, $P^{l_1l_2}_{J_{\rm A}J_{\rm a}M_{\rm a}M_{\rm A}}$, and $I^{J_{\rm A}J_{\rm B}J_{\rm a}J_{\rm b},l_2l_1l_{12}}_{JSL_{\rm tr}M_{\rm tr},s_0K}$ in Eq. (11) are given in Appendix.

Finally, for CE reactions Eq. (1) becomes

$$\frac{d\sigma}{d\Omega}(\theta) = \frac{\mu^2}{\hbar^4}\frac{(2J_{\rm B}+1)(2J_{\rm b}+1)}{(2J_{\rm A}+1)(2J_{\rm a}+1)} \sum_{\substack{JSL_{\rm tr}\\ M_{\rm tr}}} |\beta(\theta)|^2. \quad (12)$$

The partial amplitude $\beta(\theta)$ can be derived within EA, using the expressions derived above,

$$\beta(\theta) = \frac{i^{-L_{\rm tr}-M_{\rm tr}}}{(2\pi)^3} \iint dbdzbe^{i\chi(b)} J_{M_{\rm tr}}(qb) P^{M_{\rm tr}}_{L_{\rm tr}}(b,z) \times \sum_{Ks_0}\sum_{\substack{l_1l_2\\ l_{12}}} (-1)^{l_1} i^K A^K_{s_0} \hat{l}_1\hat{l}_2\hat{l}_{12}\hat{K} \times C^{l_{12}0}_{l_20l_10} C^{K0}_{L_{\rm tr}0l_{12}0} \begin{Bmatrix} S & J & L_{\rm tr}\\ l_2 & l_1 & l_{12}\\ s_0 & s_0 & K \end{Bmatrix} \times \int p^2 dp\, j_{L_{\rm tr}}(pR) F^{T_{\rm A}T_{\rm B}T_{\rm a}T_{\rm b}}_{s_0K,l_1l_2JS}(p), \quad (13)$$

with

$$F^{T_{\rm A}T_{\rm B}T_{\rm a}T_{\rm b}}_{s_0K,l_1l_2JS}(p) = C^{T_{\rm b}T_{\rm b_z}}_{T_{\rm a}T_{\rm a_z}t_0n_0} C^{T_{\rm B}T_{\rm B_z}}_{T_{\rm A}T_{\rm A_z}t_0(-n_0)} V^K_{s_0t_0}(p) D^{l_1s_0J}_{\rm AB}(p) D^{l_2s_0S}_{\rm ab}(p), \quad (14)$$

where $P^{M_{\rm tr}}_{L_{\rm tr}}(b,z)$ is the associated Legendre polynomial. This procedure, together with the incorporation of relativistic kinematics, allows for an accurate description of CE reactions in the eikonal formalism.

III. CALCULATIONS AND DISCUSSION

We now compare the EA calculations with the standard DWBA calculations, at an intermediate energy of 140 MeV/nucleon, and show the advantages of EA.

A. Calculations for partial cross sections within EA

According to Eq. (12), the total DCS for CE reactions involve the sum of all $JSL_{\rm tr}$-components. For the Gamow-Teller (GT)-type CE reactions ($J=1, S=1$) we can use the ^{120}Sn(^{3}He, t) ^{120}Sb reaction as an example. In this case, only the $JSL_{\rm tr}=110$ and 112 components are needed, corresponding to $L_{\rm tr}=0$ and $L_{\rm tr}=2$, respectively. The calculated results are displayed in Fig. 3. It can be seen that the calculations using EA and DWBA approaches agree with each other for both 110- and 112-components.

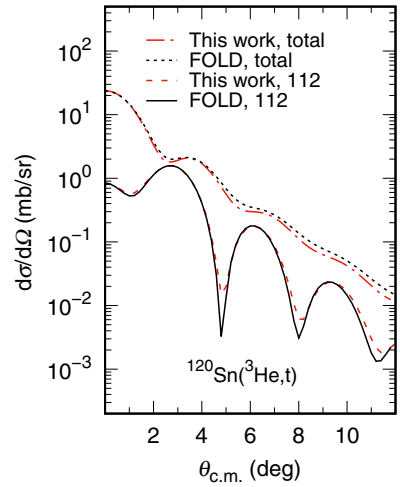

FIG. 3. Calculations for the CE reaction ^{120}Sn(^{3}He, t) ^{120}Sb at 140 MeV/nucleon by using $U_{\rm OP}$ potential [Eq. (5)] with the parameters taken from [20]. Red dashed and red dot-dashed lines represent the EA calculations for the 112-component and the total DCS, respectively. The corresponding black solid and black dotted lines are obtained with DWBA calculations using the FOLD code [20].

To clarify the contribution from different partial terms to 110- and 112-components, the cross sections [Eq. (12)] are decomposed into a series of partial waves depending on the quantum numbers s_0, K, S, J, $L_{\rm tr}$, l_1, l_2, and l_{12}, as appearing in Eqs. (A7)–(A10) and Eqs. (10)–(14). It can be seen that there are five valid contributing partial terms represented by A_1, A_2, A_3, B_1, and B_2 (A_i and B_i for 112- and 110-components, respectively, as shown in Table I). The correspondence between the A_i (B_i) coefficients and the specific quantum numbers are listed in Table I. For example, the A_1 term within EA can be expressed as

$$\frac{d\sigma}{d\Omega}_{\rm A_1}(\theta) = \frac{\mu^2}{\hbar^4}\frac{(2J_{\rm B}+1)(2J_{\rm b}+1)}{(2J_{\rm A}+1)(2J_{\rm a}+1)} \sum_{M_{\rm tr}=-2,0,2} |\beta_{\rm A_1}(\theta)|^2, \quad (15)$$

TABLE I. Values of the quantum numbers s_0, K, S, J, $L_{\rm tr}$, l_1, l_2, and l_{12}, for partial terms A_1, A_2, and A_3 related to 112-component, and B_1 and B_2 related to 110-component.

		s_0	K	S	J	$L_{\rm tr}$	l_1	l_2	l_{12}
112	A_1	1	2	1	1	2	0	0	0
112	A_2	1	0	1	1	2	2	0	2
112	A_3	1	2	1	1	2	2	0	2
110	B_1	1	2	1	1	0	2	0	2
110	B_2	1	0	1	1	0	0	0	0

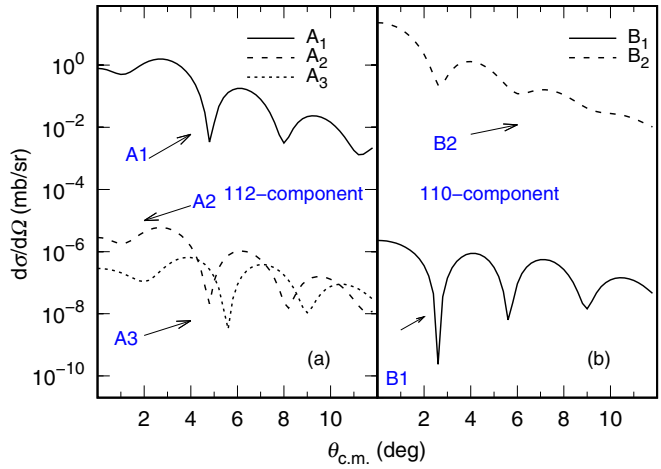

FIG. 4. For the same reaction and with the same $U_{\rm OP}$ parameters as in Fig. 3: (a) Calculated partial contributions to the DCS from the A_1 (solid line), A_2 (dashed line), and A_3 (dotted line) terms for the 112-component within EA; (b) calculated B_1 (solid line) and B_2 (dashed line) terms related to the 110-component.

with

$$\beta_{A_1}(\theta) = i^{-M_{\rm tr}} \int bdbe^{i\chi(b)} J_{M_{\rm tr}}(qb) \int dz P_2^{M_{\rm tr}}(b,z) F_{A_1}(R). \tag{16}$$

Here $P_2^{M_{\rm tr}}(b,z)$ is the associated Legendre polynomial and $F_{A_1}(R)$ the corresponding form factor in the form,

$$F_{A_1}(R) = \frac{1}{24\pi^3} \int p^2 dp j_2(pR) C^{T_b T_{b_z}}_{T_a T_{a_z} t_0 n_0} C^{T_B T_{B_z}}_{T_A T_{A_z} t_0(-n_0)} \times \tilde{V}_{11}^2(p) D^{011}_{AB}(p) D^{011}_{ab}(p). \tag{17}$$

From Fig. 4, it can be seen that 110- and 112-component DCS are dominated by B_2 and A_1 partial terms, respectively. We have also examined the transition densities in momentum space for the allowed GT decay ($s_0 = 1$, $l_1 = 0$, $J = 1$) and the second-forbidden GT decay ($s_0 = 1$, $l_1 = 2$, $J = 1$) (see Table I). Again, excellent agreements were found between EA and DWBA calculations. The transition density distributions also provide a reason for the orders of magnitude differences among the A_i (or B_i) partial contribution to the DCS.

Interestingly, comparing to A_i terms, B_i partial waves have deeper shifted first minimum [see Fig. 4(b)]. To clarify the difference between the angular distribution for A_i and B_i terms, we examined A_1 DCS which dominates over A_2 and A_3 DCS. As a matter of fact, the A_1 term is composed of three parts with magnetic quantum numbers $M_{\rm tr} = 0$ and $M_{\rm tr} = \pm 2$ [refer to Eq. (15)]. The corresponding partial DCS behave according to the Bessel functions $J_0(kb\theta)$ and $J_2(kb\theta)$, respectively, as illustrated in Fig. 5. The interference between these two contributions leads to the slow variation of DCS at small angles for the A_1 term (also for A_2 and A_3 terms). The deeper shifted first minimum for B_i partial waves (Table I) can be as well understood in this way as they depend only on the $L_{\rm tr} = 0$, and hence only on the $M_{\rm tr} = 0$ term.

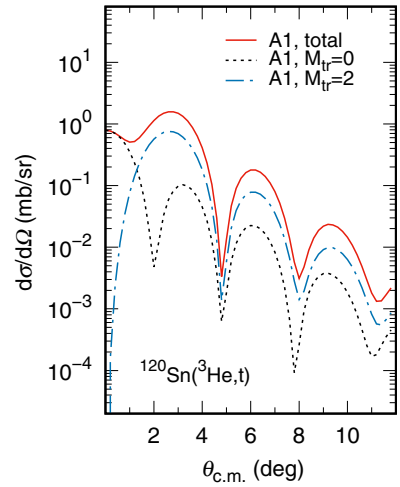

FIG. 5. For the same reaction and with the same $U_{\rm OP}$ parameters as in Fig. 3, calculated A_1 DCS within EA for $M_{\rm tr} = 0$ (black dotted line) and $M_{\rm tr} = \pm 2$ (blue dash-dotted line), respectively. The total A_1 DCS (the incoherent addition of $M_{\rm tr} = 0$ and $M_{\rm tr} = \pm 2$ items) is presented by the red solid line.

B. Effects of the tensor and exchange terms

As indicated in Sec. II, the interaction potential includes the central ($K = 0$) and tensor ($K = 2$) parts, expressed by Eqs. (A15) and (A16), respectively. Their relative importance is shown in Fig. 6. It is shown in the figure that the 110-component DCS is dominated by the central interaction whereas the 112-component DCS is dominated by the tensor interaction. As for the exchange term in the interaction [Eq. (A20)], its contribution is appreciable to the 110-component DCS, but negligible to the 112-component DCS. As a matter of fact, when we plot the real part of the potential in Fig. 7, we see an increase of the central potential depth by removing the exchange term (direct only), while no

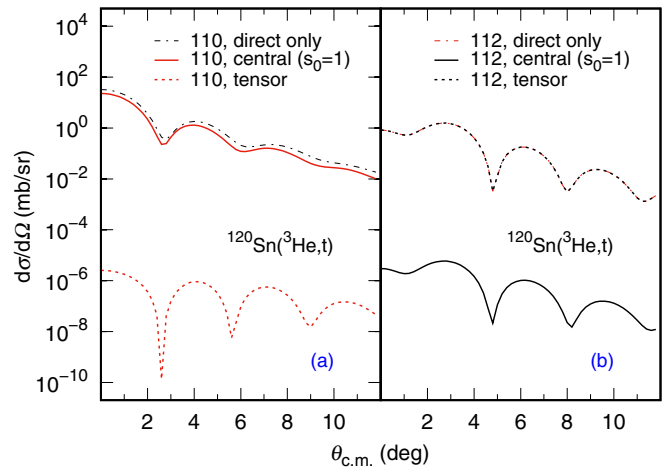

FIG. 6. For the same reaction and with the same $U_{\rm OP}$ parameters as in Fig. 3, calculated contributions to the DCS from the central (solid lines) and tensor (dotted lines) interactions, for 110-component (a) and 112-component (b). The calculations by removing the exchange term (direct only) are presented by the dash-dotted lines.

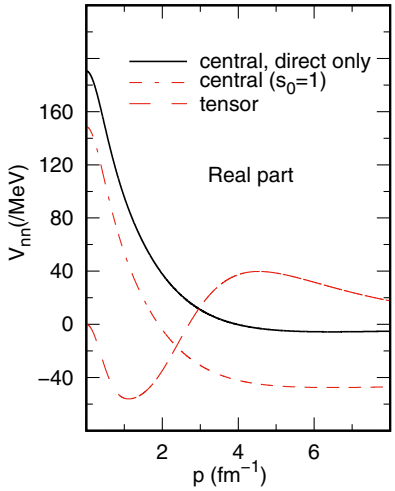

FIG. 7. The central part [Eq. (A20) for $K = 0$ and $s_0 = t_0 = 1$] and the tensor part [Eq. (A16)] of the CE interaction potential are displayed by dash-dotted line and dashed line, respectively. The black solid line represents the central potential without the exchange term [direct only, Eq. (A15)]. The exchange term has no effect on the tensor potential. Only the real parts of the potentials are presented.

change occurs for the tensor potential. Because the 110- and 112-components are dominated separately by the former and latter interactions, respectively, their contribution to the DCS changes accordingly.

C. Relativistic kinematics

To extend the application of our EA method to higher energies, relativistic kinematics for the nucleus-nucleus collision [17,19] was implemented. If v_a is the relativistic velocity of the incident particle a in the laboratory system [17], then

$$\frac{v_a^2}{c^2} = \frac{T^2 + 2Tm_0c^2}{(T + m_0c^2)^2}, \tag{18}$$

where T is the kinetic energy and m_0 the rest mass of particle a. Assuming the target nucleus A being at rest, the relativistic kinetic energy in the center-of-mass (c.m.) system [17] can be deduced from

$$E_{\rm c.m.r} = m'_A c^2 - m_A c^2 + m''_a c^2 - m_0 c^2, \tag{19}$$

where $m''_a c^2$ ($m'_A c^2$) is the total energy of the projectile (target) in the c.m. system, expressed as follows [17]:

$$m''_a c^2 = \frac{T m_A c^2 + m_0 c^2 (m_0 c^2 + m_A c^2)}{\sqrt{2T m_A c^2 + (m_0 c^2 + m_A c^2)^2}}, \tag{20}$$

or

$$m'_A c^2 = m_A c^2 \frac{T + m_0 c^2 + m_A c^2}{\sqrt{2T m_A c^2 + (m_0 c^2 + m_A c^2)^2}}. \tag{21}$$

The incident momentum for the projectile in the c.m. system k can then be expressed as [17]

$$k = \frac{m''_a v''_a}{\hbar} = \frac{m_A c^2 \sqrt{T^2 + 2Tm_0c^2}}{\hbar c \sqrt{2T m_A c^2 + (m_0 c^2 + m_A c^2)^2}}, \tag{22}$$

TABLE II. Physical quantities $E_{\rm c.m.r}$, v/c, k, and μc^2 in both relativistic (rel) and nonrelativistic (nonrel) kinematics, for the reaction ^{120}Sn(^{3}He, t) ^{120}Tn at 140 MeV/nucleon. Their absolute differences, D(%), are also shown.

	$E_{\rm c.m.r}$ (MeV)	v/c	k (fm^{-1})	μc^2 (MeV)
rel	409.026	0.497	7.827	3104.199
nonrel	409.756	0.548	7.576	2726.341
D(%)	−0.178	−9.307	3.313	13.860

where v''_a is the velocity of the projectile in the c.m. system. The velocity of the relative motion becomes [17]

$$\boldsymbol{v} = \boldsymbol{v}''_a - \boldsymbol{v}_A, \tag{23}$$

where $\boldsymbol{v}_A$ is the velocity of the target in the c.m. system. Meanwhile, the reduced mass μ is defined as [17]

$$\mu c^2 = \frac{m''_a c^2 \, m'_A c^2}{m''_a c^2 + m'_A c^2}. \tag{24}$$

Relativistic effects on the kinematic quantities are deduced and presented in Tables II and III, at 140 and 500 MeV/nucleon, respectively. In the table, we define a relative change of the momentum,

$$D = \frac{k_{\rm rel} - k_{\rm nonrel}}{k_{\rm nonrel}}, \tag{25}$$

where $k_{\rm rel}$ and $k_{\rm nonrel}$ denote k in the relativistic and nonrelativistic kinematics, respectively.

The relativistic quantities k and μ are used in the aforementioned EA calculations. To assess the effects of the corrections, we use as a benchmark the reaction ^{120}Sn(^{3}He, t) ^{120}Tn at 140 MeV/nucleon, for which the kinematical quantities are listed in Table II. The comparison between the calculations using relativistic and nonrelativistic kinematics and the same phenomenological OP, is shown in Fig. 8(a), for the total DCS and the 112-component of the DCS. It can be seen that using the proper relativistic kinematics is more important for the 112-component, although the overall effect for the total DCS is small at this relatively low energy. There is a small shift of the minimum towards the smaller angle, which is consistent with the larger k (smaller wave length) for the relativistic case. A comparison is also made between EA and DWBA calculations, both adopting relativistic kinematics [Fig. 8(b)]. The agreement is as good as for the nonrelativistic case (Fig. 3),

TABLE III. Physical quantities $E_{\rm c.m.r}$, v/c, k, and μc^2 in both relativistic (rel) and nonrelativistic (nonrel) kinematics, for the reaction ^{120}Sn(^{3}He, t) ^{120}Tn at 500 MeV/nucleon. Their absolute differences D(%) are also shown.

	$E_{\rm c.m.r}$ (MeV)	v/c	k (fm^{-1})	μc^2 (MeV)
rel	1454.186	0.775	15.922	4052.189
nonrel	1463.414	1.036[a]	14.317	2726.341
D(%)	−0.631	−25.193	11.210	48.631

[a]Just a record of the nonrelativistic kinematics.

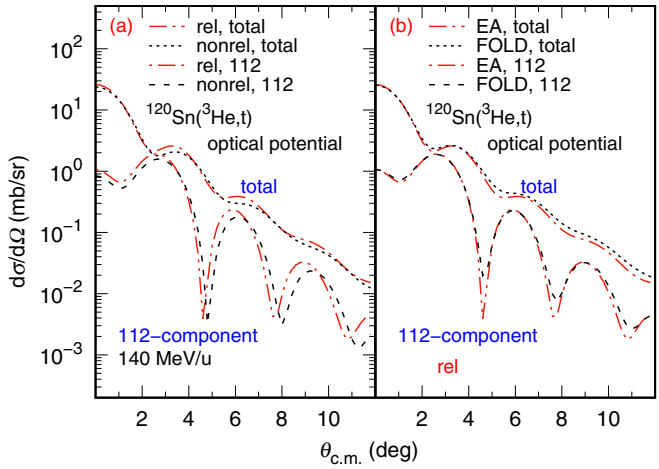

FIG. 8. (a) Comparison between calculations using relativistic and nonrelativistic (dashed and dotted lines) kinematics using EA, for the 112-component (lower lines) and the total DCS (upper lines). (b) Comparison between EA (dash-dotted lines) and DWBA (dashed and dotted lines) calculations using the FOLD code [20], both using relativistic kinematics, for the 112-component (lower lines) and the total DCS (upper lines).

indicating the consistent treatment of the relativistic kinematics in both EA and DWBA incorporated in the FOLD code.

In Fig. 9, we show the benchmark calculations for 500 MeV/nucleon. As expected, relativistic kinematic effects are much more significant at 500 MeV/nucleon (Table III) than those at 140 MeV/nucleon. Again, the 112-component is more sensitive to the kinematic corrections, as seen in Fig. 9(b).

It would be worth noting that there is a noticeable difference between the DCS calculated in OP and "$t_{\rho\rho}$" approaches, as evidenced in Figs. 8(b) and 9(a). This should be attributed to the double-folding type "$t_{\rho\rho}$" phase shift [Eq. (6)] which is somehow different from that of OP [Eq. (4)]. However,

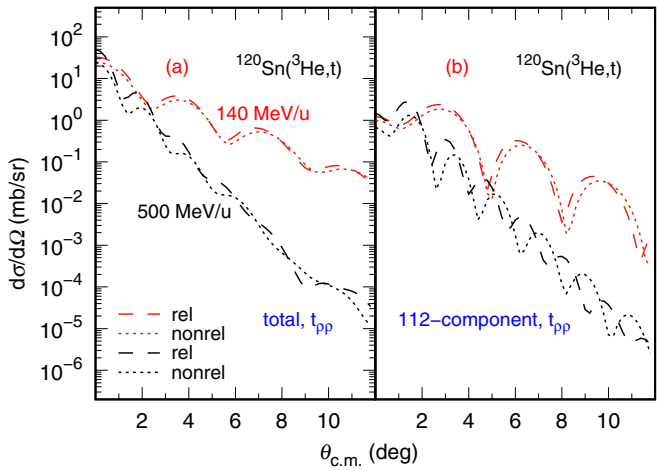

FIG. 9. (a) EA calculations of the total DCS at 500 and 140 MeV/nucleon, using relativistic (dashed lines) and nonrelativistic (dotted lines) kinematics. (b) The same as in (a) but for the 112-component DCS.

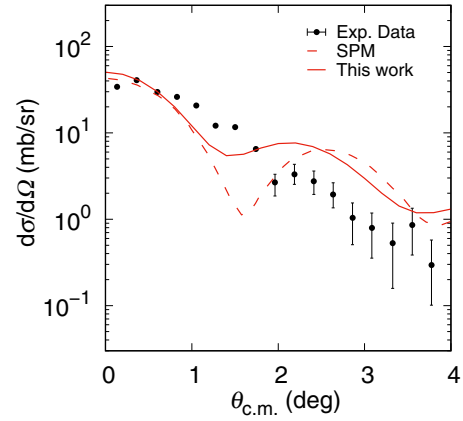

FIG. 10. Comparison of the DCS for ^{13}C (^{13}N, ^{13}C) ^{13}N reaction at 105 MeV/nucleon, between the EA calculation (solid line), the single-particle model (SPM) calculation (dashed line) [24], and the experimental data (solid circle with error bars) [21].

the DCS around 0 degrees for the two methods are quite the same, because they are sensitive only to the far surface of the potential. Because only the 0-degree DCS is essential for the current CE reaction analysis, our "$t_{\rho\rho}$" method should be valid at intermediate and high energies. Of course, further improvement of the "$t_{\rho\rho}$" method, by incorporating the medium effect in the interaction, for example, can be done in the future when DCS at larger angles are to be used.

D. Comparison with experimental data

The EA method is employed here to describe the experimental data for the mirror reaction ^{13}C(^{13}N, ^{13}C) ^{13}N at 105 MeV/nucleon [21]. The interaction potential $V^K_{s_0t_0}(r)$ at 105 MeV/nucleon is obtained through interpolation of those at 50, 100, 140, 175, 210, 270, 325, 425, 515, 650, 725, 800, and 1000 MeV/nucleon [22,23]. The OP parameters are taken from Ref. [24]. The matrix elements OBTD are calculated using the OXBASH code with the "pwt" interaction in the p-shell space [25]. As shown in Fig. 10, the EA calculation are close to the experimental results and to another calculation using the single-particle model (SPM) [24]. It is worth noting that the experimental DCS does not display an oscillatory structure because of the limited angular resolution of the detection system [21]. What is important here is the correct reproduction of the cross section at 0 degree, from which the GT transition strength can be extracted [1,26]. The actual EA calculation of $d\sigma(0^\circ_{c.m.})/d\Omega$ gives 50.43 mb/sr or 64.73 mb/sr by using the "pwt" or "ckpot" interactions, respectively, in the shell-model calculations. Both agree with the previously extracted value of 56 ± 10 mb/sr [21], within the error bars.

We also considered another example, the ^{26}Mg (^{3}He, t) ^{26}Al CE reaction [27]. EA calculations are also performed for transitions to the 1^+ state at $E_x = 1.06$ MeV and to the 0^+ isobaric analog state (IAS) at $E_x = 0.23$ MeV in ^{26}Al, respectively. The OBTD matrix elements are calculated with the OXBASH code [25] employing the "usdb" interaction in the sd-shell-model space. Single-particle wave functions are obtained from FOLD code [20]. OP parameters are taken from

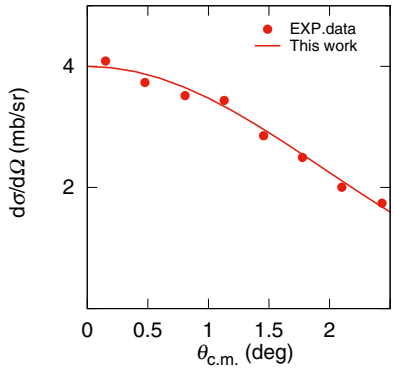

FIG. 11. Comparisons between the EA calculation (solid line) and the experimental data (solid circle) [27] for DCS of F-type CE reaction ^{26}Mg (g.s., 0^+, $T = 1$) (^{3}He, t) ^{26}Al (0.23 MeV, 0^+, $T = 1$) at 140 MeV/nucleon.

Ref. [27]. As presented in Figs. 11 and 12, the calculations, multiplied by a scaling factor of 1.330 or 0.897 for the transition to the IAS state or the 1^+ state at $E_x = 1.06$ MeV, respectively, are in good agreement with the experimental data within the measured angular range. For the present, the source of the scaling factors is still not clear and requires further investigation [27].

IV. SUMMARY

Aiming to describe heavy-ion CE reactions at intermediate energies, we have implemented the formulations and computation code within the EA approach. Calculations based on our EA method are in good agreement with the DWBA ones at 140 MeV/nucleon and also with various experimental data performed in the similar energy range.

The analysis shows that the 110- and 112-components of DCS behave according to $J_0(kb\theta)$ and $J_2(kb\theta)$, respectively. The two components of DCS are dominated by NN CE central and tensor interactions, respectively. The exchange term of the interaction also plays some visible role for the 110-component of the DCS. Relativistic kinematics has also been studied, which, as expected, exhibits a negligible effect for reactions at 140 MeV/nucleon but becomes important at 500 MeV/nucleon.

The current EA method developed here can use both phenomenological OP or microscopic developed ones, usually requiring the input of nucleon-nucleon cross sections and nuclear matter densities. Such approach has the obvious advantage that it can be applied to CE reactions at high energies (∼1 GeV/nucleon) where no OP exists. Based on the presented benchmark calculations, the EA approach is ready to be applied in the future to describe experimental data and to extract the related physics quantities, such as Gamow-Teller strengths, at energies in the range of 100 MeV/nucleon to several GeV/nucleon.

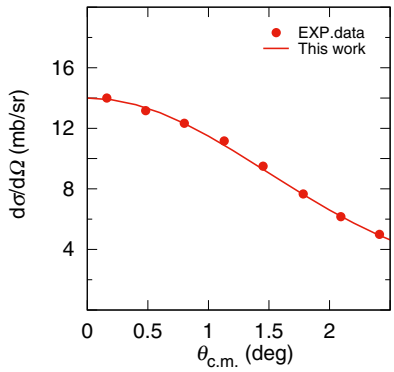

FIG. 12. Comparisons between the EA calculation (solid line) and the experimental data (solid circle) [27] for DCS of GT-type CE reaction ^{26}Mg (g.s., 0^+, $T = 1$) (^{3}He, t) ^{26}Al (1.06 MeV, 1^+, $T = 0$) at 140 MeV/nucleon.

ACKNOWLEDGMENTS

We would like to thank Prof. X. D. Tang, Y. H. Lan, and B. S. Gao for useful discussions on the measured cross sections. This work is supported by the National Key R&D Program of China (Grant No. 2018YFA0404403) and the National Natural Science Foundation of China (Grants No. 12027809, No. 11775013, No. 11875074, No. 11775004, and No. 11875073).

APPENDIX: THE FORMULAS USED IN SEC. II

The effective interaction potential V is given by [28]

$$V = \sum_{pt} V_{pt} = \sum_{pt} \sum_{s_0 t_0 K} A^K_{s_0} V^K_{s_0 t_0}(r_{pt}) \left(\tau_1^{t_0} \cdot \tau_2^{t_0}\right) \times \left[Y_K(\hat{\boldsymbol{r}}_{pt}) \cdot \left(\sigma_1^{s_0} \otimes \sigma_2^{s_0}\right)^K\right], \quad \text{(A1)}$$

where $\boldsymbol{r}_{pt}$ is the vector between the interacting target nucleon "t" and projectile nucleon "p", as indicated in Fig. 13, r_{pt} is its magnitude and $\hat{\boldsymbol{r}}_{pt}$ its associated unit vector oriented as $\boldsymbol{r}_{pt}$. In this equation, s_0 denotes the spin change of the interacting nucleons, which can have values 1 and 0, corresponding to the spin-flip and non-spin-flip processes, respectively. The isospin change t_0 has to be 1 for CE reactions. In Eq. (A1), $K = 0$ and $K = 2$ correspond to the central and tensor forces, respectively. The constants $A^K_{s_0}$ have the values $\sqrt{4\pi}$, $-\sqrt{12\pi}$, and $\sqrt{4\pi/5}$ for A^0_0, A^0_1, and A^2_1, respectively [28]. In Eq. (A1), the NN interaction strength functions $V^K_{s_0 t_0}(r)$ include both

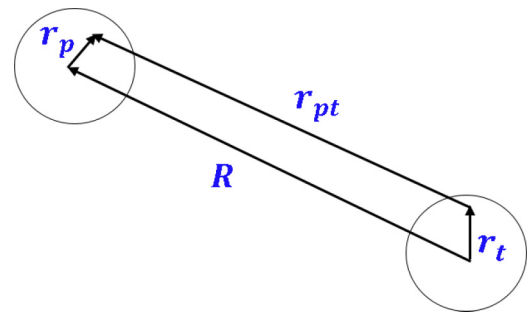

FIG. 13. The coordinates used in Eq. (A1). $\boldsymbol{R}$ is the vector between the center of mass of the reacting nuclei. $\boldsymbol{r}_p$ ($\boldsymbol{r}_t$) is the vector pointing to the nucleon p (t) from the center of the projectile (target), while $\boldsymbol{r}_{pt}$ the vector between the interacting nucleons.

the central ($K = 0$) and the tensor ($K = 2$) parts. Their parameters are taken from Refs. [22,23]. Including exchange and medium effects, the modified NN interaction strength functions are given in Ref. [22], which were adopted in the present work.

Using the following expansions,

$$\tau_1^{t_0} \cdot \tau_2^{t_0} = \sum_{n_0} (-1)^{n_0} \tau_{n_0}^{t_0}(p) \tau_{-n_0}^{t_0}(t), \tag{A2}$$

$$Y_K(\hat{\boldsymbol{r}}_{pt}) \cdot \left(\sigma_1^{s_0} \otimes \sigma_2^{s_0}\right)^K = \sum_M (-1)^M Y_{K,-M}(\hat{\boldsymbol{r}}_{pt}) \left(\sigma_1^{s_0} \otimes \sigma_2^{s_0}\right)^{KM}, \tag{A3}$$

and

$$\left(\sigma_1^{s_0} \otimes \sigma_2^{s_0}\right)^{KM} = \sum_{\nu\nu'} C^{KM}_{s_0\nu s_0\nu'} \sigma_\nu^{s_0}(p) \sigma_{\nu'}^{s_0}(t), \tag{A4}$$

the nuclear form factor $F(\boldsymbol{R})$ in Eq. (8) can be written as

$$\begin{aligned} F(\boldsymbol{R}) = \sum_{tp} \sum_{\substack{s_0 t_0 \\ K\ Mn_0}} \sum_{\nu\nu'} & \langle \Phi_{\rm B}\Phi_{\rm b} \mid V^K_{s_0 t_0}(\mid \boldsymbol{r}_p - \boldsymbol{r}_t + \boldsymbol{R} \mid) \\ & \times C^K_{s_0} (-1)^{M+n_0} C^{KM}_{s_0\nu s_0\nu'} \sigma_\nu^{s_0}(p) \sigma_{\nu'}^{s_0}(t) \tau_{n_0}^{t_0}(p) \tau_{-n_0}^{t_0}(t) \\ & \times Y_{K,-M}(\hat{\boldsymbol{r}}_{pt}) \mid \Phi_{\rm A}\Phi_{\rm a}\rangle. \end{aligned} \tag{A5}$$

At this point, it is essential to rewrite the spatial part of the interaction by introducing the δ-function notation,

$$\begin{aligned} & V^K_{s_0 t_0}(r_{pt}) Y_{K,-M}(\hat{\boldsymbol{r}}_{pt}) \\ & \quad = \int d\boldsymbol{r}_2 d\boldsymbol{r}_1 \delta(\boldsymbol{r}_2 - \boldsymbol{r}_p) \delta(\boldsymbol{r}_1 - \boldsymbol{r}_t) V^K_{s_0 t_0}(r_{21}) Y_{K,-M}(\hat{\boldsymbol{r}}_{21}). \end{aligned} \tag{A6}$$

Then $F(\boldsymbol{R})$ can be decomposed into spatial components weighted with Clebsh-Gordan (CG) coefficients,

$$\begin{aligned} F(\boldsymbol{R}) = \sum_{\substack{K s_0 \\ t_0 n_0}} \sum_{\substack{JS \\ L_{\rm tr} M_{\rm tr}}} \sum_{\substack{l_1 l_2 \\ l_{12}}} & A^K_{s_0} P^{l_1 l_2}_{J_{\rm A} J_{\rm a} M_{\rm a} M_{\rm A}} I^{J_{\rm A} J_{\rm B} J_{\rm a} J_{\rm b}, l_2 l_1 l_{12}}_{JSL_{\rm tr} M_{\rm tr}, s_0 K} \\ & \times C^{T_{\rm b} T_{\rm b_z}}_{T_{\rm a} T_{\rm a_z} t_0 n_0} C^{T_{\rm B} T_{\rm B_z}}_{T_{\rm A} T_{\rm A_z} t_0 (-n_0)} \hat{J}_{\rm b} \hat{J}_{\rm B} \hat{l}_{12} \hat{K} F^{J_{\rm A} J_{\rm B} J_{\rm a} J_{\rm b}, l_2 l_1}_{JSL_{\rm tr}, s_0 K l_{12}}(\boldsymbol{R}), \end{aligned} \tag{A7}$$

with

$$P^{l_1 l_2}_{J_{\rm A} J_{\rm a} M_{\rm a} M_{\rm A}} = (i)^{-l_1 - l_2} (-1)^{I_{\rm A} - M_{\rm A} + J_{\rm a} + m_{\rm a}}, \tag{A8}$$

$$\begin{aligned} I^{J_{\rm A} J_{\rm B} J_{\rm a} J_{\rm b}, l_2 l_1 l_{12}}_{JSL_{\rm tr} M_{\rm tr}, s_0 K} = & C^{JM_J}_{J_{\rm A} M_{\rm A} J_{\rm B} (-M_{\rm B})} C^{SM_S}_{J_{\rm a} M_{\rm a} J_{\rm b} (-M_{\rm b})} \\ & \times C^{L_{\rm tr}(-M_{\rm tr})}_{JM_J SM_S} \begin{Bmatrix} S & J & L_{\rm tr} \\ l_2 & l_1 & l_{12} \\ s_0 & s_0 & K \end{Bmatrix}, \end{aligned} \tag{A9}$$

and

$$\begin{aligned} F^{J_{\rm A} J_{\rm B} J_{\rm a} J_{\rm b}, l_2 l_1}_{JSL_{\rm tr}, s_0 K l_{12}}(\boldsymbol{R}) = & \int d\boldsymbol{r}_2 d\boldsymbol{r}_1 V^K_{s_0 t_0}(\mid \boldsymbol{r}_2 - \boldsymbol{r}_1 + \boldsymbol{R} \mid) \\ & \times \{[Y^*_{l_2}(\hat{\boldsymbol{r}}_2) Y^*_{l_1}(\hat{\boldsymbol{r}}_1)]^{l_{12}} Y^*_K(\hat{\boldsymbol{r}}_{21})\}^{L_{\rm tr}}_{M_{\rm tr}} \\ & \times D^{l_1 s_0 J}_{\rm AB}(r_1) D^{l_2 s_0 S}_{\rm ab}(r_2). \end{aligned} \tag{A10}$$

Here J (S) is the total spin transferred to the intrinsic motion of the target (projectile) system, l_1 (l_2) is the transferred orbital angular momentum of the target (projectile), l_{12} is the transferred total orbital angular momentum, $L_{\rm tr}$ is the transferred total angular momentum, and $M_{\rm tr}$ the associated magnetic quantum numbers. In Eq. (A7), $\hat{J}_{\rm b}$ has a value of $\sqrt{2J_{\rm b}+1}$, and the similar expression is true for $\hat{J}_{\rm B}$, $\hat{l}_{12}$, or $\hat{K}$. The transition densities $D^{l_1 s_0 J}_{\rm AB}(r_1)$ and $D^{l_2 s_0 S}_{\rm ab}(r_2)$ in Eq. (A10) for the target and projectile, respectively, are defined in terms of one-body transition densities (OBTD). As an example,

$$\begin{aligned} D^{l_2 s_0 S}_{\rm ab}(r) = & \sum_{\alpha\beta} R_\alpha(r) R_\beta(r) \sqrt{6(2j_\alpha + 1)} \\ & \times \langle j_\alpha \mid\mid T^{l_2 s_0 S} \mid\mid j_\beta \rangle \langle {\rm OBTD} \rangle, \end{aligned} \tag{A11}$$

where $R_{\alpha(\beta)}(r)$ is the radial part of the wave function for the initial (final) single-particle state, and $j_{\alpha(\beta)}$ and $t_{\alpha(\beta)}$ are the corresponding spin and isospin, respectively. The operator $T^{l_1 s_0 J}$ is defined as

$$T^{l_1 s_0 J}_{M_J} = \sum_{m\nu} i^{l_1} Y_{l_1 m}(\hat{\boldsymbol{r}}_t) \sigma_\nu^{s_0}(t) C^{JM_J}_{l_1 m s_0 \nu}. \tag{A12}$$

In Eq. (A11), $\langle {\rm OBTD} \rangle$ represents the reduced matrix element for the one-body operator,

$$\langle {\rm OBTD} \rangle = \frac{\langle J_b T_b \mid\mid [\hat{a}^+_{j_\alpha t_\alpha}, \tilde{a}_{j_\beta t_\beta}]^{St_0} \mid\mid J_a T_a \rangle}{\hat{S}\hat{t}_0}. \tag{A13}$$

To facilitate the practical implementation of these equations in numerical calculations, the form factor may be expressed in momentum space by using the inverse Fourier transformation for the NN interaction [refer to Eq. (A6)],

$$\begin{aligned} & V^K_{s_0 t_0}(r_{21}) Y_{K,-M}(\hat{\boldsymbol{r}}_{21}) \\ & \quad = \frac{i^K}{(2\pi)^3} \int d\boldsymbol{p} \tilde{V}^K_{s_0 t_0}(p) Y_{K,-M}(\hat{\boldsymbol{p}}) e^{-i\boldsymbol{p}\cdot(\boldsymbol{r}_2 - \boldsymbol{r}_1 + \boldsymbol{R})}. \end{aligned} \tag{A14}$$

The central and tensor terms for $\tilde{V}^K_{s_0 t_0}(p)$ are

$$\tilde{V}^0_{s_0 1}(p) = 4\pi \sum_i \frac{V^0_{s_0 1} R_i^3}{1 + (pR_i)^2}, \tag{A15}$$

and

$$\tilde{V}^2_{11}(p) = 32\pi \sum_i \frac{V^2_{11} p^2 R_i^7}{[1 + (pR_i)^2]^3}. \tag{A16}$$

The energy-dependent coefficients $V^0_{s_0 1}$ and V^2_{11} for each reaction range parameter R_i can be obtained from Ref. [22] as

$$V^0_{01} = \frac{t^{\rm SE} - 3t^{\rm TE} - t^{\rm SO} + 3t^{\rm TO}}{16}, \tag{A17}$$

$$V^0_{11} = \frac{-t^{\rm SE} - t^{\rm TE} + t^{\rm SO} + t^{\rm TO}}{16}, \tag{A18}$$

and

$$V^2_{11} = \frac{-t^{\rm TNE} + t^{\rm TNO}}{4}. \tag{A19}$$

The parameter values for $t^{\rm SE}$, $t^{\rm TE}$, $t^{\rm SO}$, $t^{\rm TO}$, $t^{\rm TNE}$, and $t^{\rm TNO}$ can be obtained from Refs. [22,23], with SE(SO) and TE(TO) denoting the singlet-even (odd) and triplet-even (odd) parts,

respectively, for the central interaction, and TNE(TNO) for the tensor interaction. The exchange term is added (for the central interaction only) according to the no-recoil approximation [27,29],

$$\tilde{V}(p) = \tilde{V}^K_{s_0 t_0}(p) \pm \tilde{V}^K_{s_0 t_0}(Q), \tag{A20}$$

where $+$ $(-)$ is for the even (odd) parts of the interaction and $Q \approx 2k\cos(\theta/2)$.

We may expand $e^{-i\boldsymbol{p}\cdot\boldsymbol{r}_2}$ and $e^{i\boldsymbol{p}\cdot\boldsymbol{r}_1}$ in Eq. (A14) using

$$e^{i\boldsymbol{p}\cdot\boldsymbol{r}} = 4\pi \sum_{\mathrm{LM}} i^L j_L(pr) Y^*_{LM}(\hat{\boldsymbol{p}}) Y_{LM}(\hat{\boldsymbol{r}}). \tag{A21}$$

The form factor in Eq. (A10), including the NN interaction and the transition densities, can then be expressed in momentum space as

$$F^{J_\mathrm{A} J_\mathrm{B} J_\mathrm{a} J_\mathrm{b}, l_2 l_1}_{J S L_\mathrm{tr}, s_0 K l_{12}}(\boldsymbol{R}) = \sum_{\substack{m_1 m_2 \\ M_{12} M}} \frac{i^{l_1 - l_2 + K}}{(2\pi)^3} C^{L_\mathrm{tr} M_\mathrm{tr}}_{l_{12} m_{12} l_1 m_1} C^{l_{12} m_{12}}_{l_2 m_2 l_1 m_1} \int d\boldsymbol{p} Y^*_{KM}(\hat{\boldsymbol{p}}) \tilde{V}^K_{s_0 t_0}(p) \times Y^*_{l_2 m_2}(\hat{\boldsymbol{p}}) Y^*_{l_1 m_1}(\hat{\boldsymbol{p}}) e^{-i\boldsymbol{p}\cdot\boldsymbol{R}} D^{l_1 s_0 J}_{\mathrm{AB}}(p) D^{l_2 s_0 S}_{\mathrm{ab}}(p). \tag{A22}$$

The transition densities are

$$D^{l_1 s_0 J}_{\mathrm{AB}}(p) = \sum_{\alpha\beta} 4\pi \sqrt{6(2j_\alpha + 1)} \langle j_\alpha \,||\, T^{l_1 s_0 J} \,||\, j_\beta \rangle \langle \mathrm{OBTD} \rangle \times \int dr\, j_{l_1}(pr) r^2 R_\alpha(r) R_\beta(r), \tag{A23}$$

and similarly for $D^{l_2 s_0 S}_{\mathrm{ab}}(p)$.

[1] R. G. T. Zegers *et al.*, Phys. Rev. Lett. **99**, 202501 (2007).
[2] S. Noji *et al.*, Phys. Rev. Lett. **120**, 172501 (2018).
[3] D. Frekers, M. Alanssari, H. Ejiri, M. Holl, A. Poves, and J. Suhonen, Phys. Rev. C **95**, 034619 (2017).
[4] A. Brockstedt *et al.*, Nucl. Phys. A **530**, 571 (1991).
[5] D. L. Prout *et al.*, Phys. Rev. C **63**, 014603 (2000).
[6] X. Roca-Maza, G. Colò, and H. Sagawa, Phys. Rev. Lett. **120**, 202501 (2018).
[7] D. Frekers, P. Puppe, J. Thies, and H. Ejiri, Nucl. Phys. A **916**, 219 (2013).
[8] J. Yasuda *et al.*, Phys. Rev. Lett. **121**, 132501 (2018).
[9] H. Lenske, H. H. Wolter, and H. G. Bohlen, Phys. Rev. Lett. **62**, 1457 (1989).
[10] C. A. Bertulani, Nucl. Phys. A **554**, 493 (1993).
[11] C. A. Bertulani, C. M. Campbell, and T. Glasmacher, Comput. Phys. Commun. **152**, 317 (2003).
[12] A. Etchegoyen *et al.*, Phys. Rev. C **38**, 2124 (1988).
[13] A. Etchegoyen, D. Sinclair, S. Liu, M. Etchegoyen, D. Scott, and D. Hendrie, Nucl. Phys. A **397**, 343 (1983).
[14] B. T. Kim, A. Greiner, M. A. G. Fernandes, N. Lisbona, K. S. Low, and M. C. Mermaz, Phys. Rev. C **20**, 1396 (1979).
[15] F. Petrovich and D. Stanley, Nucl. Phys. A **275**, 487 (1977).
[16] J. S. Winfield, N. Anantaraman, Sam M. Austin, L. H. Harwood, J. van der Plicht, H.-L. Wu, and A. F. Zeller, Phys. Rev. C **33**, 1333 (1986).
[17] Y. Suzuki, R. G. Lovas, K. Yabana, and K. Varga, *Structure and Reactions of Light Exotic Nuclei* (Niigata, Japan, 2003).
[18] R. J. Glauber, *Lectures in Theoretical Physics*, edited by W. E. Brittin *et al.* (Interscience, New York, 1959), Vol. 1, p. 315.
[19] C. A. Bertulani and P. Danielewicz, *Introduction to Nuclear Reactions* (IOP, Bristol and Philadelphia, UK, 2004).
[20] https://people.nscl.msu.edu/∼zegers/fold/fold_package.tar.
[21] M. Steiner *et al.*, Phys. Rev. Lett. **76**, 26 (1996).
[22] W. G. Love and M. A. Franey, Phys. Rev. C **24**, 1073 (1981).
[23] M. A. Franey and W. G. Love, Phys. Rev. C **31**, 488 (1985).
[24] C. A. Bertulani and P. Lotti, Phys. Lett. B **402**, 237 (1997).
[25] B. A. Brown *et al.*, *NSCL* Report No. MSUCL-1289 (2004).
[26] F. Osterfeld, N. Anantaraman, S. M. Austin, J. A. Carr, and J. S. Winfield, Phys. Rev. C **45**, 2854 (1992).
[27] R. G. T. Zegers *et al.*, Phys. Rev. C **74**, 024309 (2006).
[28] C. A. Bertulani, arXiv:1510.00491.
[29] T. Udagawa, A. Schulte, and F. Osterfeld, Nucl. Phys. A **474**, 131 (1987).